Dynamics of femtosecond laser-induced melting of silver

Wai-Lun Chan,[1,*] Robert S. Averback,[1] David G. Cahill,[1] and Alexei Lagoutchev[2]
[1]*Department of Materials Science and Engineering, University of Illinois at Urbana–Champaign, Urbana, Illinois 61801, USA*
[2]*School of Chemical Science, University of Illinois at Urbana–Champaign, Urbana, Illinois 61801, USA*
(Received 4 August 2008; revised manuscript received 10 November 2008; published 17 December 2008; corrected 19 December 2008)

We use optical third-harmonic generation to measure the melting dynamics of silver following femtosecond laser excitation. The dynamics reveals an unusual two-step process that is associated with the extreme electronic temperatures and very short time and length scales. In the first, which lasts a few picoseconds, the electron and phonon systems begin to equilibrate, and a thin surface layer undergoes melting. Heat conduction during this period is strongly suppressed by electron scattering from *d*-band excitations. In the second stage, the surface region remains above the melting temperature for a surprisingly long time, 20–30 ps, with the melt front propagating into the bulk at a velocity of ≈ 350 m s^{-1}. In this stage, the electron and phonon systems again fall out of equilibrium and conduction of heat away from the surface region is now limited by the weak electron-phonon (*e-p*) coupling. From our model calculation, we propose that the melt depths in noble metals irradiated by femtosecond lasers are limited to thicknesses on the order of two to three times of the optical-absorption depth of the light.

DOI: 10.1103/PhysRevB.78.214107 PACS number(s): 64.70.D−, 61.80.Ba, 72.15.Eb, 78.47.J−

I. INTRODUCTION

Over the last two decades, femtosecond laser has been used extensively to study ultrafast melting of different materials.[1–4] Unlike traditional melting in which both electrons and phonons are heated simultaneously, a characteristic of femtosecond laser melting is that the electrons can reach temperatures on the order of 10 000 K before they transfer their energy to the phonon system. Recent studies have used ultrafast x-ray[2] or electron diffraction[3,4] to probe melting, but with the exception of computer simulations,[5,6] these studies have explored the initial homogeneous melting and have not considered situations where the melt front propagates beyond the absorption depth of the laser light. The kinetics of ultrafast melting in thick films (>100 nm), however, is more complex, since it depends intimately on the physics of nanoscale heat transport at extremely high electron temperatures and temperature gradients. Heat transport under such conditions—e.g., when the spatial extent of the temperature gradient is smaller than the mean-free path of the heat carriers[7]—is an area that is poorly understood, despite its importance for such technologies as femtosecond laser machining[8] or ion-beam irradiation.[9]

In this work, we measure ultrafast melting kinetics in Ag and analyze the results using a two-temperature model[10] (TTM); comparisons between the model and the experimental results enable us to probe the physics of heat conduction on nanometer scales. For the experiments, third-harmonic (TH) light generation is used as a probe which enables us to measure the speed of the liquid-solid interface quantitatively, an important quantity that to our knowledge has not been previously measured during femtosecond laser melting. We find several interesting features in the melting kinetics. First, the melting threshold is nearly independent of film thickness for thickness as small as 75 nm; implying most of the heat is confined in the top ≈ 50 nm of the film. This heat confinement cannot be explained by the current models of heat transport in noble metals. Second, the melting consists of two stages. Homogeneous melting occurs in the first few picoseconds. Then the liquid-solid interface moves steadily into the bulk at a velocity of 350 m s^{-1} for another 25–30 ps. The second stage is surprising considering the high heat conductance of Ag and the thickness of the melted layer ($\approx 20-30$ nm).

In our analysis using TTM, we include the effects of *d*-band excitations on electron transport, in addition to its effects on electron heat capacity and *e-p* coupling.[4,11–13] We propose that the heat confinement observed in experiment is due to the scattering of the conduction electrons by the *d*-band holes, when the electron system is highly excited in the first two picoseconds. After the cooling of the hot electrons during *e-p* equilibration, the *e-p* coupling time increases dramatically. This leads to electron and phonon systems again falling out of equilibrium, but now with hot phonons and cold electrons. This limits the heat transport from the melted region and prolongs the melting for another 20–30 ps. Finally, from our TTM, we argue that the strong initial heat confinement limits the depth of material that can be melted to approximately equal to two to three times of the optical-absorption depth before ablation sets in at higher fluences.

II. EXPERIMENTAL RESULTS

The melting is studied with a typical pump-probe setup using a 800 nm laser with a pulse width of 140 fs. A pump pulse with fluence in the range of $0-0.5$ J cm^{-2} is used to excite the thin-film specimens. A time-delayed probe, with a beam diameter ten times smaller than the pump pulse, is positioned at the center of the pump beam to determine the amount of liquid that is present on the surface. TH generation provides a convenient probe for melting, since a circularly polarized beam of light results in TH generation in crystalline samples with fourfold symmetry, but it does not generate a TH signal in isotropic materials such as liquids.[14] Details of this method can be found in Ref. 15. Since the TH

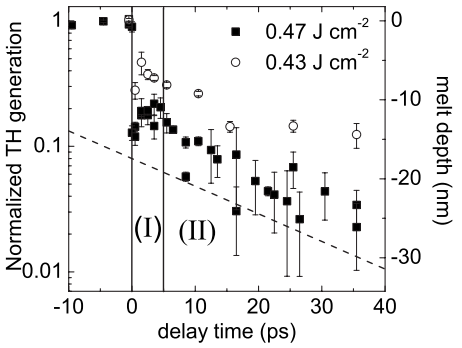

FIG. 1. Normalized TH generation as a function of delay time for a 200 nm Ag film. The axis on the right shows the corresponding melt depth. The melting can be divided into two stages: (I) initial melting due to transfer of energy from electron to phonon and (II) propagation of the melting front into the superheat solid. The dotted line represents a melting speed of 350 $m\ s^{-1}$. All the experimental data are taken by a single shot. Each data point represents the average of at least three independent measurements. The error bar represents the standard deviation of these measurements.

generation is proportional to the third power of the beam intensity, a high probe fluence, 0.61 $J\ cm^{-2}$, is needed to generate enough signal for single shot experiments. The high fluence causes damage in the crystals. Nevertheless, because any structural damage takes place after the TH signal is generated, the signal reports on the structure of the crystal before it is damaged by the probe beam.

The samples are epitaxial Ag (001) films that were sputter deposited on MgO (001) substrates in a vacuum chamber with base pressure of $\approx 3 \times 10^{-8}$ Torr. The sample is grown at 200 °C, using a growth rate of 7.9 $nm\ min^{-1}$. A 1-nm-thick Fe (001) film is deposited between the substrate and the Ag films to ensure that the Ag grows epitaxially. X-ray diffraction confirms that the films are single crystalline. Film thicknesses varied from 50 to 200 nm.

A. Melting kinetics

Figure 1 shows measurements performed on a 200-nm-thick Ag film on a MgO substrate using two different pump fluences. The pump fluences are slightly higher than the melting threshold. The TH intensity is normalized to the intensity generated by the same probe beam without the pump beam. An intensity equal to one thus represents an unexcited solid. In the first few picoseconds following excitation, labeled as stage I in Fig. 1, the TH signal drops rapidly. In this stage, the TH signal is influenced by the initial, high electron temperature, which explains the local minimum that appears near $t \approx 0$ ps. At the end of this stage, $t \approx 5$ ps, most of the heat transferred from electron to phonon systems has occurred and a melted region is formed. The duration of this stage is consistent with previous electron-diffraction experiments performed on 20-nm-thick Au.[4]

After the initial rapid melting, the melt front propagates steadily into the bulk (stage II in Fig. 1). Since the liquid phase does not generate TH light, the depth of the melt $d(t)$ can be related to the normalized intensity I through the exponential relationship

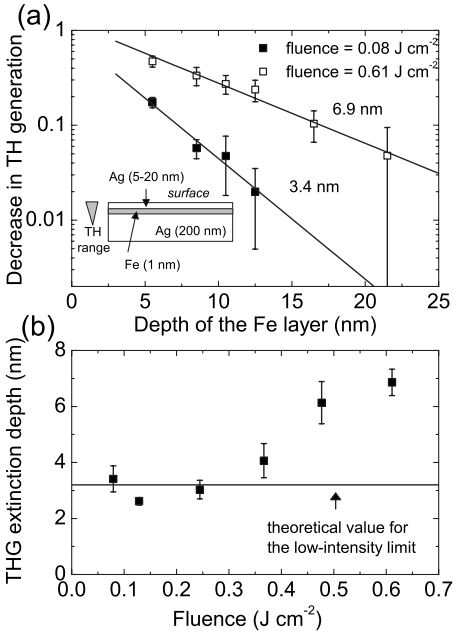

FIG. 2. (a) The decrease in TH signal as a function of the depth of the Fe layer for two probe fluences. The slope in the figure represents the extinction depth for the TH generation. The inset is a schematic of the samples used in the calibration experiment. (b) The extinction depth for TH generation as a function of probe fluence.

$$I(t) = \exp\left[-d(t)\left(\frac{3}{d_{\mathrm{I}}} + \frac{1}{d_{\mathrm{III}}}\right)\right], \tag{1}$$

where d_{I} and d_{III} are the extinction depths of the fundamental and TH light. The factor of 3 in the exponential term arises from the cubic dependence of the TH signal on the probe-laser intensity. Equation (1) neglects the difference in the dielectric constant between the liquid and solid phase. This, however, is a good approximation for metals such as Ag, for which the two phases have a very similar dielectric constants.[16] The slope of the logarithmic plot in Fig. 1 thus represents the velocity of the melt front. The combined extinction depth $(3/d_{\mathrm{I}}+1/d_{\mathrm{III}})^{-1}$, represents a characteristic depth from which the signal is generated, and at low laser fluence, it can be determined by the dielectric constant. For high laser fluences, however, this depth is not known *a priori*, and therefore we measured it separately.

The calibration was done by measuring the TH intensity for a series of Ag films (of a total thickness ≈ 200 nm) with a 1 nm Fe layer embedded at depths ranging from 5 to 20 nm beneath the surface. The Ag (001) and Fe (001) layers are grown epitaxially. A schematic of the sample is shown as an inset in Fig. 2(a). Since Fe has a much weaker TH yield compared to Ag for 800 nm light, the TH generation from a sample with an Fe layer (I_{Fe}) is weaker than the TH generation from a sample without the Fe layer (I_0). The influence of the Fe layer on TH generation diminishes exponentially with its depth below the surface. If we plot $(1-I_{\mathrm{Fe}}/I_0)$ against the depth of the Fe layer in a semilogarithmic scale, the slope represents the extinction depth of the TH generation. The result of the decrease in TH generation as a function of the

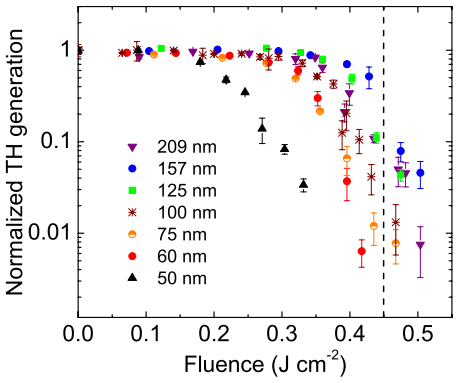

FIG. 3. (Color online) TH generation as a function of pump fluence for different film thicknesses. The delay time is fixed at 25 ps.

depth of the Fe layer is shown in Fig. 2(a). The measured extinction depth is 6.9 ± 0.5 nm for the probe fluences we are using (0.61 J cm^{-2}). Using the same method, we found the extinction depth to be 3.4 ± 0.5 nm at 0.08 J cm^{-2}—the low intensity limit. This value is in good agreement with the theoretical value, 3.2 nm, calculated from the known dielectric constant of Ag and Eq. (1). The combined extinction depth as a function of fluence is shown in Fig. 2(b). The extinction depth agrees with the theoretical value until the fluence is larger than 0.3 J cm^{-2}.

Using our measured extinction depth, we convert the TH signal into the melt depth (shown in the axis on the right in Fig. 1). We find that the average melt-in velocity over the period $t=5$ ps to $t=25$ ps is ≈ 350 m s^{-1} (represented by the dashed line in Fig. 1). The amount of Ag melted in stage II is comparable to stage I. The combined maximum melt depth for both stages is $\approx 25-30$ nm, which occurs at $t \approx 30$ ps.

We find no evidence of ablation using the above fluences. This conclusion derives from a comparison of the x-ray intensities generated in a secondary electron microscope from the Ag film before and after laser irradiation. This comparison showed that the ablation is less than 1 nm per pulse, demonstrating that the melt threshold in Ag is lower than the ablation threshold. For laser fluences higher than 0.55 J cm^{-2}, however, we found that the irradiated portion of the film detached from the substrate.

B. Dependence of the melting threshold on film thickness

In order to estimate the depth of the initial heat deposition, we repeat the same experiment with different film thicknesses (50–200 nm). Electrons can carry heat away from the optical extinction depth before they couple to the phonons. This measurement characterizes the dynamics of these "hot" electrons. Similar ideas have been used in Refs. 17 and 18 to study the fast electron transport at lower fluences. In these experiments, we fix the delay time at 25 ps, which is short relative to the time for resolidification, and measure the TH intensity as a function of pump fluence. The results are shown in Fig. 3. The film does not melt until a threshold is reached. The amount of melt then increases approximately linearly with respect to the additional fluence. The threshold for melting and the amount of melt remain nearly independent of film thickness, until the thickness falls below 100 nm. Since the melting threshold should decrease and the amount of melt should increase when the film thickness is smaller than the depth of heat deposition, assuming negligible heat transport across the Ag-MgO interface in 25 ps, the result indicates that at $t=25$ ps, most of the heat is confined within the top 50–100 nm.

Experiments performed at lower fluences[17–19] have indicated that hot electrons can carry heat a few times deeper than what we observe here. The electron dynamics, as we shall discuss, thus changes when the fluence is high enough to induce melting. A previous study on Au shows that the damage threshold increases linearly with the film thickness for a thickness up to 500 nm, which apparently contradicts to our results. However, the threshold reported in Ref. 20 is determined from the cumulative damages in a multishot experiment. The absorbed fluence per pulse in the actual experiment is at least three to four times lower than the melting threshold. The electron temperature reached by these studies is therefore lower than that attained in our films. In particular, the *d*-band electrons were not excited in Ref. 20. This further suggests the importance of the excitation of *d*-electrons on heat transport.

In Sec. II A, we observe a two-stage melting in Ag thin films excited by femtosecond laser. The depth of heat deposition is surprising shallow (<100 nm). In the following, we use a TTM to understand what aspects of the heat transport can create the spatial confinement observed in Fig. 3. The model is not aimed at being rigorous since such a treatment on the electron transport with *d*-band excitation that includes the consideration of nonequilibrium electrons is beyond the scope of this paper. The model is used to estimate the amount of heat confinement induced by excited *d*-band holes and to explore possible heat confining mechanisms. In the second part of the discussion, we use the TTM model to demonstrate how the heat confinement can produce the two-stages melting observed experimentally. Note that the reconstruction of the melting kinetics is mainly based on a surface heat confinement that is experimentally observed in Fig. 3, but as it will be seen, it is insensitive to the details of the actual heat confining mechanisms.

III. HEAT CONFINEMENT DUE TO *d*-BAND EXCITATION

A. TTM

TTM is commonly used to model the laser heating of metals.[4,11–13,18] The accuracy of the model depends on the physical parameters employed, such as the *e-p* coupling constant and the heat diffusivities from both electrons and phonons at high electron temperature. We do not discuss the TTM in detail, which can be found in many references, e.g., Refs. 11–13 and 18, but rather focus on the parameters used in our model since they differ from those commonly used in TTM. Here, we highlight that while previous TTMs include the effects of *d*-band excitation on *e-p* coupling constant and heat capacity[4,11–13] they have not considered the scattering of conducting *s*-band electrons with *d*-band holes. The *d*-band

excitation, however, will significantly lower the electron-scattering time and heat conductivity . We will show that the decrease in κ_e by d-band scattering is essential for causing the heat confinement observed experimentally.

First, we use the e-p coupling constant g and electron heat capacity C_e calculated in Ref. 13 since this work includes d-band excitations. g is multiplied by a constant to ensure it agrees with the experimental value (3.5×10^{16} W m^{-3} K^{-1}, Ref. 21) measured at room temperature. Note that g is now temperature dependent, and C_e is no longer proportional to temperature. These values are a consequence of the excitation of d-band electrons.

The heat conductivity κ_e is modeled using the Drude model. The scattering time includes both e-p and electron-electron (e-e) scatterings. The conductivity is given by

$$\kappa_e = \frac{T_e}{(A_{ep}T_p + A_{ee}T_e^2)}, \tag{2}$$

where T_e and T_p are the electron and phonon temperatures, A_{ep} and A_{ee} represent the scattering term due to e-p and e-e scatterings. The T_e dependence in the numerator derives from C_e of the *conducting electrons*. Only s electrons are considered in the transport processes, owing to the high effective mass of d electrons.[22] This should be distinguished from the C_e in the TTM described above, which represents the heat capacity of all the electrons (i.e., both s and excited d electrons) that can be thermalized. Furthermore, we assume that C_e of s electrons is linear in T_e. This does not account for the additional s electrons that are excited from the d band. Since the number of such excitations only increases the total number of s electrons by $\approx$10%. A_{ep} is taken to be the inverse of heat conductivity at room temperature, which is 0.0025 m K W^{-1}.

While the coefficient A_{ee} is usually assumed to be constant,[11–13,18] we note that owing to the excitation of d electrons at high T_e [($T_e>4000$ K (Ref. 13)], the e-e scattering is greatly enhanced. Indeed, scattering of s electrons is far more effective with d-band holes than with other s electrons because of the high effective mass of d-band holes.[22] For example, A_{ee} of Ni is about 2 orders of magnitude higher than that of Ag because Ni has d-band holes but Ag does not.[22] To account for the effect of d-band holes on electron scattering, we add the contribution of s-d scattering to the total scattering rate by the following phenomenological relationship,

$$A_{ee} = A_{ee,0}[1 + CN_h(T_{el})]. \tag{3}$$

In this equation, $A_{ee,0}$ is the e-e scattering coefficient in the low-temperature limit, which for Ag is 0.13 m MW^{-1}, Ref. 23. N_h is the number of d-band holes per atom, which is determined by integrating the Fermi distribution.[24,25] The constant C represents the ratio of the s-d electron-scattering rate to the s-s electron-scattering rate; we roughly estimate that $C=150$, based on A_{ee} being about 2 orders of magnitudes larger in Ni than in Ag, with the number of effective d-band holes in Ni$\approx$0.6.[22,23,26] Equation (3) is generally valid for other noble metals.

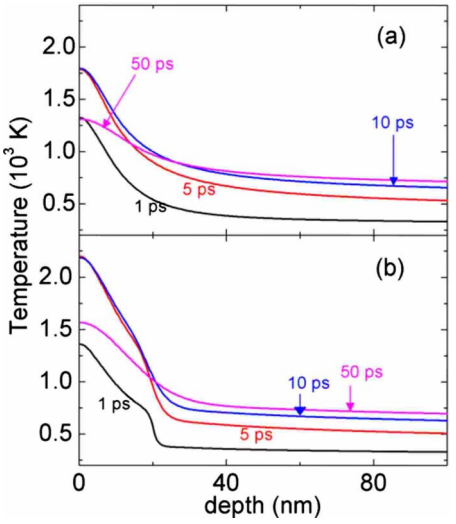

FIG. 4. (Color online) (a) Calculated phonon temperature from the TTM at different delay times (only the top 100 nm is shown). The film thickness is 200 nm and the absorbed fluence is 0.025 J cm^{-2}. Additional e-e scattering by d-band holes, modeled by Eq. (3), is included in the TTM. (b) An effective interface impedance ($G=8$ GW m^{-2} K^{-1}, see the text) is added to the calculation in (a) in order to account for the nonlocal effect of the d-band holes.

The phonon conductivity κ_p is normally 2 orders of magnitude smaller than κ_{el}, and usually ignored in TTMs, but we keep the phonon conduction term here and set $\kappa_p=6.7\times(298/T_p)$ W m^{-1} K^{-1} (estimated using κ_p of Ni measured by molecular dynamic (MD) simulation[27] and the formalism reported in Ref. 28). As we will discuss in the text, this term becomes significant when heat is transported over small dimensions. The laser energy is deposited in Ag using an optical extinction depth of 12 nm, which is calculated from the dielectric constant of Ag. Transmission and reflectance measurements made in this work show no significant increase in the extinction depth for the 800 nm pump pulse at the fluence that we are using. We do not include ballistic transport in our model. Although ballistic transport can be observed at low electron excitation,[17,18,29] this effect is largely suppressed in our case since both e-p and e-e scattering rates increases by an order of magnitude when d electrons are excited. This significantly lowers the mean-free path of the electrons.

The TTM is solved by standard finite-differencing method, using a step size=0.4 nm and time step=0.004 fs. Our model does not include melting and the latent heat of transformation, and the difference in thermodynamic and transport properties between the liquid and solid phases is neglected. The consequences of these approximations are discussed below.

B. Results from the TTM

Figure 4(a) shows the calculated phonon temperature T_p as a function of depth for five different times. The thickness of the film is 200 nm, and the absorbed fluence is 0.025 J cm^{-2}. The absorbed fluence used in the model is estimated by an experimental measurement on the reflectiv-

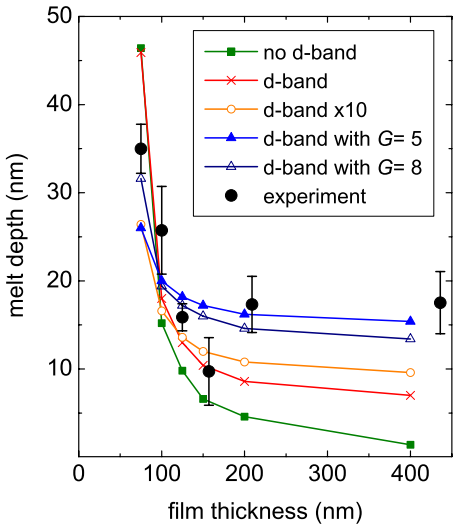

FIG. 5. (Color online) Melt depth as a function of film thickness at delay time equals to 25 ps. The experimental points (black solid circles) are determined from Fig. 3, at fluence=0.45 J cm^{-2} (the vertical dashed line in Fig. 3). For the TTM calculation, the absorbed fluence is fixed at 0.025 J cm^{-2}. The modeling parameters used are green line with squares—no enhancement in *e-e* scattering rate from *d*-band holes [$C=0$ in Eq. (3)]; red line with crosses—enhancement in *e-e* scattering modeled by Eq. (3), with $C=150$; orange line with open circles—$C=1500$; and blue lines with triangles—$C=150$, with the addition of an effective interface impedance G (see the text). Only $G=5$ and 8 GW m^{-2} K^{-1} are shown.

ity of the pump beam. In Fig. 4(a), we can see that some heat is confined at the surface and the remainder is distributed uniformly in the film. In order to quantify whether the model agrees with the thickness dependence shown in Fig. 3, we plot the melt depth (d) at $t=25$ ps as a function of film thickness. In the TTM, d can only be estimated from the thermal history of the films as melting is not explicitly included in the TTM. We thus define d as the midpoint between the maximum depth of the sample at which phonon temperature is larger than 1234 and 1620 K in the first 25 ps. The former temperature is the melting temperature T_m, and the latter temperature is chosen to include the latent heat of melting L. (A material can melt homogenously if $T>T_m+L/C_p$, where C_p is the heat capacity.) For the experiments, d is determined from Fig. 3 at a fluence equal to 0.45 J cm^{-2} (the vertical line in Fig. 3).

The results from experiments and modeling are shown in Fig. 5 as black circles and a red line (with crosses), respectively. In the experiments, d does not vary significantly for thicknesses larger than 125 nm. In contrast, d calculated by the model continues to decrease until the film thickness reaches 200 nm. Furthermore, the decrease in d from thin (75 nm) to thick (>200 nm) films is far more pronounced in the model than in the experiments. This rapid decrease in d with film thickness illustrates that most of the energy is distributed uniformly in the film [corresponding to the background temperature in Fig. 4(a)]. When the film thickness increases, less heat remains in the near-surface region and the melt depth decreases. The discrepancy appears resolvable only if a larger temperature gradient exists at the surface region, i.e., a larger fraction of the heat is confined to the surface region. Increasing the *s-d* electron-scattering rate [C in Eq. (3)], even by an order of magnitude, decreases d for the 75 nm film, but it does not significantly increase the melt depth for the thicker films (the orange line with open circles in Fig. 5). In addition, at this high value of C, the surface phonon temperature reaches 3000–4000 K, for which ablation should take place,[30] but is not observed in our experiments. If we neglect the effects of d electrons on heat conduction, as in other TTMs,[4,11–13,18] the agreement between experiments and models is far worse and the film heats nearly uniformly. These results are shown as the green line (with solid squares) in Fig. 5.

We next explore possible additional mechanisms that can create the heat confinement necessary to explain the experimental results; we do this by adding a thermal interface impedance. This is rationalized by recognition of the sharp interface that is created by the *d*-band excitations in the surface region. Since a large temperature gradient [see Fig. 4(a)] exists over a distance that is small compared to the electron mean-free path, λ, of Ag (e.g., $\lambda\approx 50$ nm at RT[31]), κ_e on the "cold" side of the interface is overestimated in the above TTM. In other words, the excited *d*-band electrons should have influence on κ_e in the unexcited region, extending to a distance on the order of λ. A similar argument for nonlocal heat transport was employed previously in Refs. 7 and 32 to describe the reduction in phonon conductivity when the curvature in the temperature depth profile is large. We place the interface at a depth of 20 nm and assume its conductance varies inversely with the number of *d*-band holes. Since the number of *d*-band holes increases approximately linearly with electron temperature T_e above some critical temperature ($\approx$4000 K), we take the interface conductance as $10\,000\times G/(T_s-4000)$, where T_s is the surface temperature. In the first 3–4 ps, T_s falls from around 15 000 K to a temperature below 4000 K. Therefore, the interface is only active during stage I, shown in Fig. 1. We vary G from 2 to 12 GW m^{-2} K^{-1}. The evolution of T_p of a 200 nm film in our TTM, now with the addition of the interface impedance, is shown in Fig. 4(b). The melt depth as a function of film thickness is shown in Fig. 5 (blue lines with triangles). The prediction of the model now agrees well with the experiment for $G\approx 5-8$ GW m^{-2} K^{-1}. For comparison, we note that the conductance of Cu-Al interface is 4 GW m^{-2} K^{-1},[33] and a conductance of 8 GW m^{-2} K^{-1} effectively reduces κ_e in a 50-nm-thick region in Ag by half.

Our model thus demonstrates that the inclusion of scattering of conduction electrons from excited *d*-band holes and the nonlocal effects created by extremely large temperature gradients described above can reconcile the heat confinement necessary to explain the present experiments. Next, we show that this heat confinement is consistent with the two-stages melting observed experimentally.

IV. TWO STAGES OF MELTING DYNAMICS

We can now reconstruct the melting scenario. In Fig. 6, we plot the isotherms in the sample in which T_p equals to

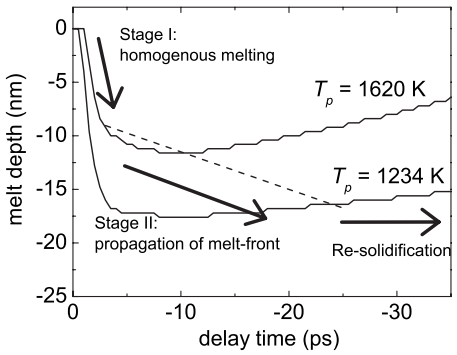

FIG. 6. Constant temperature contours at 1234 and 1620 K calculated by TTM. The parameters used are same as in Fig. 4(b). In stage I melting, the solid melt homogenously along the $T=1620$ K contour. In stage II, the melt front propagates within these two contours. The dashed line represents a melting speed of 350 m s^{-1}.

1234 and 1620 K as a function of time. For regions in the sample for which $T_p > 1620$ K, we assume that they melt immediately because there is no energy barrier to melting. This treatment is consistent to the observations in MD simulations, which show that metals melt homogenously for $T_p > 1.2T_m$.[6,34] In the first few picoseconds, the surface temperature increases rapidly. The top 10 nm of sample melt homogenously in less than 5 ps. The initial melting stage is comparable to stage I in Fig. 1; the duration of this stage is controlled by the *e-p* coupling time. Heat confinement is maintained in this stage by the scattering of conduction electrons from the excited *d*-band holes. Without this heat confinement, the melt depth in stage I can be much larger.

In stage II ($t \approx 5-25$ ps), the melt front should propagate into the bulk (within the two temperature contours in Fig. 6) as heat from the surface region diffuses in. Note that the constant-temperature contours can retract to the surface as the sample cools down, but the melting front should only move forward and eventually stop when the temperature of the front is less than T_m. This is because the resolidification is much slower than the melting. Indeed, resolidification does not start until $t > 50$ ps, where we see a slow recovery of the TH signal in the experiments (not shown in the figures). It is difficult to determine precisely the melt-in velocity from our TTM since the temperature near the surface spans a range of 700 K. We can interpolate the position of melt front, however, by using the experimental melt-in velocity (350 m s^{-1}). This is indicated by the dashed line in Fig. 6. The melting stops as the temperature of the front falls below T_m, which occurs at $t \approx 20-25$ ps. This is consistent with the experiment in which the melting continues until t ≈ 30 ps. Notably, the velocity measured in the experiment is slightly higher than the heterogeneous melting velocity observed in MD,[6] which indicates that part of the melting in stage II must occur homogenously. Furthermore, if latent heat is included in the model, we expect that the surface temperature and the overall temperature gradient will be decreased by $\approx 300-400$ K. This can slow the cooling and slightly increase the duration of stage II.

Figure 6 illustrates that the surface region remains at high temperatures (above T_m) long after the *d*-band excitations have subsided; the duration of stage II melting, therefore, is quite long, as observed experimentally in Fig. 1. This indeed is surprising, considering Ag regains its high thermal conductivity in this stage. For example, using the heat diffusivity of Ag at the melting point, the heat within a 30 nm region can be removed in 6 ps. This estimate, however, neglects the time required for the heat in the phonon system to transfer to the electrons, and for a very thin hot layer, the slow *e-p* coupling limits the cooling rate. This can readily be observed from the results of the TTM. For the calculation shown in Fig. 4(b), T_e at the surface is just ≈ 100 K higher than T_e at back for $t > 5$ ps, regardless of the larger gradient in T_p. While different transport processes are included implicitly in the TTM, we can illustrate the phenomenon more clearly by calculating the effective conductance for heat carried away from a hot region of thickness h through electron G_e and phonon G_p. The effective heat conductance for phonons, by dimensional analysis, is equals to κ_p/h (κ_p is phonon heat conductance). A thinner surface hot layer (i.e., smaller h) implies a steeper temperature gradient, which increases the effective heat conductance.

The conductance for electrons is more complicated. Heat must first be transferred from phonons in the hot surface layer to electrons, and it is carried away by electrons through diffusion. The transfer of heat back into the phonon system in the cold region is not the rate limiting process, assuming the cold reservoir is always much thicker than the hot region. The first step depends on the *e-p* coupling constant and is proportional to the thickness of the hot layer. The conductance for this step is $G_{e\text{-}ep}=gh$. The conductance for the second step (electron diffusion) is $G_{e\text{-}d}=\kappa_e/h$. The conductance of electrons is the combination of the two conductances in series, which is given by

$$G_e = \frac{1}{(G_{e\text{-}ep}^{-1} + G_{e\text{-}d}^{-1})} = \frac{1}{1/gh + h/\kappa_e}. \tag{4}$$

Normally $G_{e\text{-}ep} \gg G_{e\text{-}d}$, which gives $G_e \approx G_{e\text{-}d}$. However, for small h and g, $G_{e\text{-}ep}$ can be small enough such that it will dominate the heat transport. In our case, taking $h=25$ nm yields $G_{e\text{-}d} \approx 16$ GW m^{-2} K^{-1} and $G_{e\text{-}ep} \approx 0.9$ GW m^{-2} K^{-1}. It is thus clear that G_e is limited by *e-p* coupling, and its value calculated by Eq. (4) is 0.85 GW m^{-2} K^{-1}. In addition, this small value of G_e is the same order of magnitude as the phonon conductance G_p. Using κ_p in our model, we find $G_p=0.27$ GW m^{-2} K^{-1}. Although G_p is still smaller than G_e, it is no longer negligible as most studies have assumed.[4,11,12,18] The phonon conduction, moreover, becomes increasingly more important as h falls below 25 nm.

The heat confinement has significant implications for the amount of material that can be melted by femtosecond laser irradiation. The excitation of *d*-band electrons in stage I limits the depth of the initial heat deposition to approximately the optical-absorption depth of the material. Subsequently, transport of heat by electrons from the excited region in stage II is limited by the weak *e-p* coupling. Although this limitation lengthens the melt lifetime, it is ineffective in increasing the total melt depth since most of the heat removed from the surface layer is evenly redistributed over the re-

mainder of the film, i.e., a large temperature drops in the hot region is compensated for by a small temperature rise in the cold region. Increasing the laser fluence does not increase the melt depth appreciably since the extra energy results in ablation before the heat can spread into the bulk. For example, we have found that in our MD simulations, a Cu lattice becomes unstable at $T_p \approx 4000$ K (i.e., ablation will occur).[35] Since the surface phonon temperature in our TTM calculation already reaches 2000 K and the heat confinement increases nonlinearly as the laser fluence increases, we estimate that the maximum melt thickness in Ag is not larger than 30–40 nm before ablation becomes significant.

V. CONCLUSION

In conclusion, we have examined the melting kinetics in Ag. The melting consists of two stages. The first stage is homogenous melting with duration controls by the *e-p* coupling time. In the second stage, the melting front propagates into the bulk and the dynamics is determined by how heat is dissipated from the initially hot surface region. The results give us important insight into the heat transport under high electron excitation and the melting dynamics of a superheated solid. The proposed picture should hold for other noble metals such as Au and Cu.

ACKNOWLEDGMENTS

We acknowledge the support from U.S. DOE-NNSA under Grant No. DEFG52-06NA26153 and the U.S. DOE-BES under Grants No. DEFG02-05ER46217 and No. DEFG02-07ER46459. Sample characterization was carried out in part in the Frederick Seitz Materials Research Laboratory Central Facilities, University of Illinois, which are partially supported by the U.S. Department of Energy under Grants No. DE-FG02-07ER46453 and No. DE-FG02-07ER46471.

*wlchan@uiuc.edu

[1] C. V. Shank, R. Yen, and C. Hirlimann, Phys. Rev. Lett. **50**, 454 (1983); C. Guo, G. Rodriguez, A. Lobad, and A. J. Taylor, *ibid.* **84**, 4493 (2000); S. I. Ashitkov, M. B. Agranat, P. S. Kondratenko, S. I. Anisimov, V. E. Fortov, V. V. Temnov, K. Sokolowski-Tinten, B. Rethfeld, P. Zhou, and D. von der Linde, JETP Lett. **76**, 461 (2002); M. Kandyla, T. Shih, and E. Mazur, Phys. Rev. B **75**, 214107 (2007).

[2] C. W. Siders, A. Cavalleri, K. Sokolowski-Tinten, Cs. Toth, T. Guo, M. Kammler, M. Horn von Hoegen, K. R. Wilson, D. von der Linde, and C. P. J. Barty, Science **286**, 1340 (1999); A. Rousse, C. Rischel, S. Fourmaux, I. Uschmann, S. Sebban, G. Grillon, Ph. Balcou, E. Forster, J. P. Geindre, P. Audebert, J. C. Gauthier, and D. Hulin, Nature (London) **410**, 65 (2001); K. Sokolowski-Tinten, C. Blome, C. Dietrich, A. Tarasevitch, M. Horn von Hoegen, D. von der Linde, A. Cavalleri, J. Squier, and M. Kammler, Phys. Rev. Lett. **87**, 225701 (2001); K. J. Gaffney *et al.*, *ibid.* **95**, 125701 (2005); A. M. Lindenberg *et al.*, *ibid.* **100**, 135502 (2008).

[3] B. J. Siwick, J. R. Dwyer, R. E. Jordan, and R. J. Dwayne Miller, Science **302**, 1382 (2003); M. Harb, R. Ernstorfer, C. T. Hebeisen, G. Sciaini, W. Peng, T. Dartigalongue, M. A. Eriksson, M. G. Lagally, S. G. Kruglik, and R. J. Dwayne Miller, Phys. Rev. Lett. **100**, 155504 (2008).

[4] R. Ernstorfer, M. Harb, T. Dartigalongue, C. T. Hebeisen, R. E. Jordan, L. Zhu, and R. J. Dwayne Miller, in *Ultrafast Phenomena XV*, Springer Series in Chemical Physics Vol. 88, edited by P. Corkum, D. J. Dwayne Miller, D. M. Jones, and A. M. Weiner (Springer, Berlin, 2007), pp. 755-757.

[5] P. Lorazo, L. J. Lewis, and M. Meunier, Phys. Rev. B **73**, 134108 (2006).

[6] D. S. Ivanov and L. V. Zhigilei, Phys. Rev. Lett. **98**, 195701 (2007); Z. Lin, R. A. Johnson, and L. V. Zhigilei, Phys. Rev. B **77**, 214108 (2008).

[7] G. D. Mahan and F. Claro, Phys. Rev. B **38**, 1963 (1988).

[8] X. Liu, D. Du, and G. Mourou, IEEE J. Quantum Electron. **33**, 1706 (1997).

[9] C. P. Flynn and R. S. Averback, Phys. Rev. B **38**, 7118 (1988); Z. G. Wang, Ch. Dufour, E. Paumier, and M. Toulemonde, J. Phys.: Condens. Matter **6**, 6733 (1994).

[10] S. I. Anisimov, B. L. Kapeliovich, and T. L. Perel'man, Sov. Phys. JETP **39**, 375 (1974).

[11] X. Y. Wang, D. M. Riffe, Y.-S. Lee, and M. C. Downer, Phys. Rev. B **50**, 8016 (1994).

[12] A. N. Smith and P. M. Norris, Appl. Phys. Lett. **78**, 1240 (2001).

[13] Z. Lin, L. V. Zhigilei, and V. Celli, Phys. Rev. B **77**, 075133 (2008).

[14] P. N. Butcher and D. Cotter, *The Elements of Nonlinear Optics* (Cambridge University Press, Cambridge, 1990).

[15] B. C. Gundrum, R. S. Averback, and D. G. Cahill, Appl. Phys. Lett. **91**, 011906 (2007).

[16] J. C. Miller, Philos. Mag. **20**, 1115 (1969).

[17] C. Suarez, W. E. Bron, and T. Juhasz, Phys. Rev. Lett. **75**, 4536 (1995).

[18] J. Hohlfeld, J. G. Muller, S.-S. Wellershoff, and E. Matthias, Appl. Phys. B: Lasers Opt. **64**, 387 (1997); M. Bonn, D. N. Denzler, S. Funk, M. Wolf, S. Svante Wellershoff, and J. Hohlfeld, Phys. Rev. B **61**, 1101 (2000).

[19] G. Tas and H. J. Maris, Phys. Rev. B **49**, 15046 (1994).

[20] S.-S. Wellershoff, J. Gudde, J. Hohlfeld, J. G. Miller, and E. Matthias, Proc. SPIE **3343**, 378 (1998); S.-S. Wellershoff, J. Hohlfeld, J. Gudde, and E. Matthisa, Appl. Phys. A: Mater. Sci. Process. **69**, S99 (1999).

[21] R. H. M. Groeneveld, R. Sprik, and A. Lagendijk, Phys. Rev. B **51**, 11433 (1995).

[22] N. F. Mott and H. H. Wills, Proc. R. Soc. London, Ser. A **153**, 699 (1936); W. G. Baber and H. H. Wills, *ibid.* **158**, 383 (1937).

[23] A. H. MacDonald and D. J. W. Geldart, J. Phys. F: Met. Phys. **10**, 677 (1980).

[24] The *d* band is assumed to be a rectangular band with the upper edge 3.3 eV below the Fermi level and the width is 3.33 eV. A parabolic *s* band is used with density of state at the Fermi level equal to 0.11 $\text{atom}^{-1}\,\text{eV}^{-1}$ (based on Ref. 25).

[25] G. Fuster, J. M. Tyler, N. E. Brener, J. Callaway, and D.

Bagayoko, Phys. Rev. B **42**, 7322 (1990).
[26] T. L. Ruthruff, C. G. Grenier, and R. G. Goodrich, Phys. Rev. B **17**, 3070 (1978).
[27] X. Zheng, D. G. Cahill, P. Krasnochtchekov, R. S. Averback, and J.-C. Zhao, Acta Mater. **55**, 5177 (2007).
[28] G. A. Slack, in *Solid State Physics*, edited by H. Ehrenreich, F. Seitz, and D. Turnbull (Academic, New York, 1979), Vol. 34, p. 1.
[29] X. Liu, R. Stock, and W. Rudolph, Phys. Rev. B **72**, 195431 (2005).
[30] D. S. Ivanov and L. V. Zhigilei, Phys. Rev. B **68**, 064114 (2003).
[31] C. Kittle, *Introduction to Solid States Physics*, 7th ed. (Wiley, New York, 1996).
[32] Y. K. Koh and D. G. Cahill, Phys. Rev. B **76**, 075207 (2007).
[33] B. C. Gundrum, D. G. Cahill, and R. S. Averback, Phys. Rev. B **72**, 245426 (2005).
[34] A. B. Belonoshko, N. V. Skorodumova, A. Rosengren, and B. Johansson, Phys. Rev. B **73**, 012201 (2006); F. Delogu, J. Phys.: Condens. Matter **18**, 5639 (2006).
[35] N. Q. Vo and R. S. Averback (unpublished).